X-ray multimodal imaging using a random-phase object

Sebastien Berujon,[1,2,*] Hongchang Wang,[1] and Kawal Sawhney[1]

[1]*Diamond Light Source, Harwell Science and Innovation Campus, Didcot, Oxfordshire OX11 0DE, England*
[2]*European Synchrotron Radiation Facility, BP-220, F-38043 Grenoble, France*

We demonstrate an extension of the x-ray grating interferometer three modal imaging method to a generalized stepping scheme using a phase object with small, random features. The method allows the recovery of the absorption, scattering, and two-dimensional phase image of the sample from a raster scan of the phase object. An additional extension of the method to recover the effective wave-front curvature is also described. The technique provides fine sensitivity and high spatial resolution and has only low requirements on spatial and longitudinal coherence of the x-ray beam. Imaging modes and processing methods are explained, and an experimental demonstration of the technique is provided by imaging a feather and the quantitative characterization of a compound refractive lens.

I. INTRODUCTION

Imaging has been one of the main applications of x rays since their discovery. While the highly penetrating nature of x rays is commonly used to reveal the interior of material objects, the scientific community has also exploited the short wavelength of x rays to image sample features down to the nm scale. To achieve high spatial resolution or image light material, new x-ray imaging techniques exploiting the phase of the waves were developed over the two last decades [1]. One such technique is x-ray grating interferometry.

The use of x-ray grating interferometers (XGIs) has quickly spread following the adaptation of the device from visible optics [2,3] to hard x rays [1,4,5] and the demonstration of coherence mapping. Today, a large community takes advantages of this device using both synchrotron and laboratory sources [6,7]. Indeed, its imaging capabilities make it very attractive: in addition to an absorption map of the sample, it also provides the phase shift and the scattering map induced by the sample [8] on an x-ray beam.

The phase shift corresponds to both the delay and the local angular deflection on the photon beam propagation by the sample. Recovering this valuable information directly permits the deduction of the refractive index δ of the sample. Such information is of particular interest for low atomic number material where the value of δ is many orders of magnitude larger than the absorption factor β of the optical index $n = 1 - \delta - i\beta$.

For many years grating interferometers were limited to the measurement of the phase gradient in only one direction due to the technical challenges in fabricating two-dimensional gratings. However, the issue has recently been overcome [9], allowing the recovery of the two directional phase map in a single scan. A few researchers also reported the possibility of using XGIs in a magnification geometry in an attempt to improve the spatial resolution of the device for imaging purposes [10,11].

The idea of mapping the scattering properties of an object came out only a few years after the extension of the grating interferometer to the x-ray regime [8]. The principle is to calculate the local reduction of the coherence which arises from small angle scattering in the sample. The mapping of this scattering effect is also sometimes called a dark-field image and reflects the degree of inhomogeneity at the nm scale inside the sample.

A schematic of an XGI is shown in Fig. 1. The grating interferometer is also sometimes called the "shearing interferometer" because it relies first on a phase grating to split or "shear" the beam into two diffracting orders. The two parts of the beam then interfere further downstream from the phase grating, creating a fringe pattern. The position and amplitude of these interference fringes allow the calculation of the phase shift and absorption of the sample. Often the pixel size of the detector is larger than the grating period, and placing a second absorbing grating with a tuned pitch in front of the detector creates larger resolvable Moiré fringes due to the aliasing effect. For accurate phase retrieval, the XGI is usually used in a scanning mode where several images are acquired while moving one of the gratings relative to the other in a plane transverse to the beam. In interferometry such a process is called phase stepping [12]. From these images, Fourier methods are used to recover the beam gradient through the fringe phase calculation.

The fabrication of the XGI's gratings is a technical challenge [13], especially when the gratings are designed to work at high energy. The grating lines are required to have a period of a few microns to achieve good sensitivity and spatial resolution of the device. At the same time, the aspect ratio need to be very high to induce a phase shift large enough to produce a workable contrast, leading to line depths ranging from 15 μm to more than 100 μm when designed to introduced π phase shift at high energy [14]. These gratings are usually made by XUV lithography on silicon substrate. The second absorbing grating has its lines filled with heavy elements, such as gold deposited by electroplating. Hence, the grating pitch limits the spatial resolution of the interferometer, while the absorption of the device at lower x-ray energies can sometimes also become an issue. Finally, as one might expect, the quality of the grating can also affect the results [15].

In spite of the advantages of the XGI, researchers are still exploring and developing improved or derived methods

---

*sebastien.berujon@diamond.ac.uk
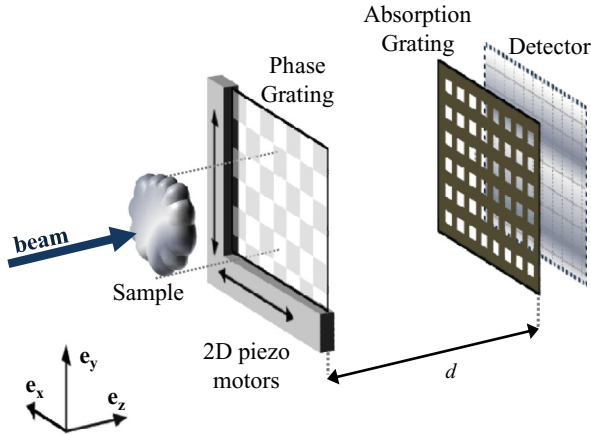
FIG. 1. (Color online) Schematic of a two-dimensional x-ray grating interferometer. Gratings are placed in an x-ray beam downstream from a sample to create an interference pattern. The distortion of this pattern from the one obtained when no sample is inserted into the beam permits the recovery of the phase shift induced by the sample.

[16,17]. These efforts are motivated by the desire to image matter at ever higher spatial resolutions while diminishing and minimizing the x-ray dose delivered to the sample.

A new x-ray beam phase sensing technique has recently been developed for imaging and metrology purposes: this technique [18,19] relies on the use of x-ray near-field speckle [20] combined with cross-correlation algorithms. In addition to several other advantages, the technique has been shown to provide a few tens of nanoradians sensitivity in the measurement of wave-front gradients, and spatial resolution on the micron scale. Despite promising possibilities for imaging using the differential mode, in which the contribution of the sample on the phase of the x-ray beam is isolated, the technique suffers from several drawbacks, including: measurements are limited by the magnification of the speckle upon propagation while using the absolute mode to recover the effective phase of the beam; the spatial resolution of the technique is limited by the size of the speckle grains; and finally scattering maps are not accessible, unlike with an XGI.

We propose a generalized method, derived from the XGI that uses any phase generated pattern or speckle rather than a periodic grating. A simple membrane with random features replaces the phase grating. Using a complete mathematical description of the stepping scheme, we show that the requirement of a grating with a perfectly known pitch, as employed in the XGI, is not essential. The method provides the two-dimensional beam phase gradient, employs a simple setup, and achieves higher spatial resolution than the current XGI devices. It is also shown that the XGI is a special case of the generalized method presented.

II. THEORY

A. Basis

The concept of this paper is to consider a sample as a time invariant system represented as a transfer function h, which is linked to the optical index n of the sample. For the following, we consider a monochromatic beam propagating

through a sample in the z direction of a frame $(\mathbf{x},\mathbf{y},\mathbf{z})$ and with transverse coherence lengths of the order or smaller than the sample features. Placing an imaging detector downstream of the sample, the intensity collected I_{det} at a point $T = (x_0,y_0)$ will be equal to the square modulus of the probing wave u_0 convoluted with the optical transfer function $h_T(x,y) = h(x_0,y_0,x,y)$ [21,32]:

$$I_{\text{det}}(x_0,y_0) = |u(x_0,y_0)|^2$$

$$= \left| \iint_{-\infty}^{+\infty} h(x_0,y_0,x,y)u_0(x,y)dxdy \right|^2$$

$$= \iiiint_{-\infty}^{+\infty} h_T(x_1 - x_0, y_1 - y_0)h_T^*(x_2 - x_0, y_2 - y_0)$$

$$\times \langle u_0(x_1,y_1)u_0^*(x_2,y_2)\rangle dx_1 dy_1 dx_2 dy_2. \quad (1)$$

One approximation is made for the following treatment: the small transverse coherence length of the beam is neglected and the field correlation function $\langle u(x_1,y_1)u^*(x_2,y_2)\rangle = I_0(\frac{x_1+x_2}{2}, \frac{y_1+y_2}{2})\psi_0(x_1 - x_2, y_1 - y_2)$ is taken as incoherent illumination. This means that $\psi_0(x_1 - x_2, y_1 - y_2) \approx \kappa\delta(x_1 - x_2, y_1 - y_2)$ with δ representing the Dirac distribution. While this approximation for the width of the function ψ_0 does not affect the beam phase sensing, the partial coherence of the x-ray beam will be responsible for some edge contrast in the absorption image. Denoting $\mathscr{F}$ as the Fourier transform operator, Eq. (1) can be then written using the convolution theorem and the two functions $\mathscr{F}[|h|^2] = H$ and $\mathscr{F}[|u_0|^2] = \tilde{I}_0$ [21,32]:

$$I_{\text{det}}(x_0,y_0) = \kappa \iint_{-\infty}^{+\infty} |h_T(x - x_0, y - y_0)|^2 I_0(x,y)dxdy$$

$$= \mathscr{F}^{-1}[\kappa H(x_0,y_0,\xi,\nu)\tilde{I}_0(\xi,\nu)]. \quad (2)$$

The way to recover the optical transfer function h of the sample is to feed the system with a reference signal $|u_0|^2$, which is a two-dimensional (2D) pattern, and compare this with the signal collected at the exit of the system. Figure 2 schematically describes this scheme which is a common problem in physics and signal processing. More precisely, it consists of estimating the transfer function $H(x_0,y_0,\xi,\nu) = H_T(\xi,\nu)$ of the sample which is applied to the reference signal, and to do so for each pixel T determined by the index pair (k,l):

$$H_{kl} = \frac{\tilde{g}_{kl}^{\text{samp}}}{\tilde{g}_{kl}^{\text{ref}}}, \quad (3)$$

where the operator $\sim$ denotes the Fourier transform of the function $\tilde{g} = \mathscr{F}[g(x,y)](\xi,\nu)$. The functions $g^{\text{ref}}(x,y)$ and $g^{\text{samp}}(x,y)$, respectively, describe the 2D optical intensity
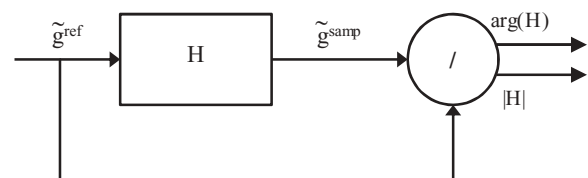
FIG. 2. Processing representation.

recorded when the sample is out of the beam (flat field reference) and when the sample is introduced into the beam. These functions reflect physical recorded signals and are then bounded by a finite subspace Γ of size $\Gamma_x \times \Gamma_y$. Thus, the Fourier transform is treated in the following in the exponential Fourier series limit:

$$\tilde{g}(\xi,\nu) = \frac{1}{\Gamma} \int_\Gamma g(x,y) e^{-i2\pi(\xi x + \nu y)} dx\, dy, \qquad (4)$$

with $\xi = p/\Gamma_x, \nu = q/\Gamma_y, (p,q) \in \mathbb{Z}^2$ the set of integers.

We show how to recover $|H|$, which represents the absorption and decrease of coherence brought about by the sample, and also demonstrate that the argument $\arg(H)$ relates to the beam gradient.

B. Stepping scheme

Instead of considering a grating producing interference, consider a phase object with high frequency features creating local phase shifts on a partially coherent wave front. As with many propagation based contrast imaging techniques [22–24], the object will create interference contrast after propagation over a short distance z due to the local curvature of the beam. This phenomena can be described by the transport of intensity equation [25]:

$$\frac{2\pi}{\lambda} \frac{\partial I}{\partial z} = -\nabla \cdot (I \nabla \varphi), \qquad (5)$$

with λ the wavelength. In Eq. (5), I is the recordable intensity and ∇ represents the transverse nabla operator in the plane $(\mathbf{x},\mathbf{y})$ perpendicular to the beam propagation direction z. The phase of the beam is φ, and a surface defined by $\varphi(x,y,z) = cst$ is the wave front W.

When interferences arise from spatially uncorrelated features, it creates a random interference pattern called speckle [26]. With hard x rays and up to a certain propagation distance, a more specific form of speckle is obtained: the "near-field speckle." This kind of speckle, used here, has been demonstrated to be closely related to the form and structure of the scattering object [20].

The experimental setup consists of mounting a phase object with small features, downstream of a removable sample, on a piezo motor that allows translation in the two transverse directions of the x-ray beam. Likewise, a 2D detector able to resolve the near-field speckle pattern is placed into the beam. In this manner one can perform the so-called stepped two-dimensional raster scan of the phase object. In the following, each scan consists of $M \times N$ points, defining a surface Γ of the high frequencies phase modulating scanned object.

Performing such scans, one records image stacks defining a four-dimensional signal, which is used to recover the transfer function. Indeed, performing two similar raster scans, one with the sample in the beam, and the other without the sample, one obtains two sets of 2D data for each pixel: (k,l): g_{kl}^{samp} when the sample is in the beam; and g_{kl}^{ref} when the sample is removed (this is often referred to as the flat field reference).

The average intensity μ, the standard deviation σ, and the energy ε collected in a recorded pattern g in a given pixel are defined by

$$\mu = \frac{1}{\Gamma} \int_\Gamma g = \tilde{g}(0,0), \quad \sigma = \sqrt{\frac{1}{\Gamma} \int_\Gamma (g - \mu)^2},$$

$$\varepsilon^2 = \sum_{-\infty}^{+\infty} |\tilde{g}|^2 = \int_\Gamma |g|^2. \qquad (6)$$

C. Absorption imaging

An absorption image is defined as the ratio of the number of photons falling on a pixel of the detector with and without the sample present in the x-ray beam. Retrieval of the attenuation A image is calculated by taking the ratio of the energy collected in each pixel in the scans:

$$A(k,l) = 1 - \frac{\varepsilon_{kl}^{samp}}{\varepsilon_{kl}^{ref}} \qquad (7)$$

Because the x rays are only partially coherent, most of the recorded signal comes from noninterfering, background light. Using the approximation $\varepsilon \approx \mu$, one can retrieve the formulas based on the use of the Fourier transformed signals:

$$A(k,l) \approx 1 - \frac{\mu_{samp}}{\mu_{ref}} = 1 - \frac{\left| \tilde{g}_{kl}^{samp}(0,0) \right|}{\left| \tilde{g}_{kl}^{ref}(0,0) \right|} = 1 - |H(0,0)|. \qquad (8)$$

D. Phase imaging

In the hard x-ray regime, due to the weak interaction of the photons with matter, deflection angles induced by the refraction are usually very small, i.e., much less than a degree. When an object is introduced into the x-ray beam, the propagation direction of the light will be slightly changed, and the speckle pattern recorded will be modified relative to its reference "version" when no sample was present. This idea is the basis of many deflection angle techniques, such as the Hartmann sensor [27], the x-ray speckle tracking technique [18], or the XGI [28] in which wave-front gradients are measured through the displacement of an intensity modulation pattern. The deflection angle α is equal to the wave-front gradient $\alpha = |\nabla W|$, and the transverse local shift $\mathbf{v}$ of the pattern will be equal to [29]

$$\mathbf{v} = d\nabla W = d\frac{\lambda}{2\pi} \nabla \varphi, \qquad (9)$$

where d is the propagation distance from the reference phase objet to the detector. Hence, the recovery of the shift $\mathbf{v}$ between recorded signals as shown in Fig. 3 can lead to the knowledge of α and the local beam phase.

Here, the recovery of $\mathbf{v}$ is achieved using Eq. (3) by separating the amplitude and phase of the transfer function H:

$$\tilde{g}_{kl}^{samp} = H_{kl} \tilde{g}_{kl}^{ref} = |H_{kl}| \tilde{g}_{kl}^{ref} e^{-i\delta\Phi_{kl}}. \qquad (10)$$

In this expression, the argument of H, $\delta\Phi(\xi,\nu) = \arg[H(\xi,\nu)]$ is, according to the shift theorem, the delay between the two signals g^{ref} and g^{samp}. A traditional method to derive this phase component is to use the 2D cross-correlation operation with the two recorded signals. Dropping the pixel subscripts for the sake of clarity, and separating the orthogonal
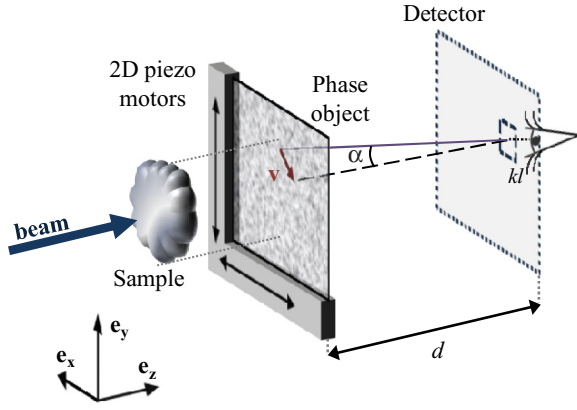
FIG. 3. (Color online) Schematic of a generalized stepping imaging setup. A phase object with small features is mounted on a 2D piezo motor beyond the sample, and a highly resolving detector is placed at a distance d. The 2D raster scan of the scattering object allows one to calculate the scattering vector v for each pixel when the sample is introduced into the beam.

components of $\delta\Phi(\xi,\nu) = \delta\Phi_x(\xi) + \delta\Phi_y(\nu)$, we have

$$g_{\text{samp}} \star g_{\text{ref}} = \tilde{g}_{\text{samp}}^* \cdot \tilde{g}_{\text{ref}}$$
$$= |H(\xi,\nu)||\tilde{g}_{\text{ref}}(\xi,\nu)|^2 e^{-i[\delta\Phi_x(\xi)+\delta\Phi_y(\nu)]}, \quad (11)$$

where $\star$ denotes the correlation operator, and $*$ the complex conjugate. Using the phase in the exponential part of this last equation, one can deduce **v** from the shift theorem:

$$\mathbf{v} = \frac{\delta\Phi_x(\xi)}{2\pi\xi}\mathbf{e_x} + \frac{\delta\Phi_y(\nu)}{2\pi\nu}\mathbf{e_y}. \quad (12)$$

And finally combining Eqs. (9) and (12), one can calculate the beam phase gradient in the two orthogonal directions:

$$\frac{\partial\varphi}{\partial x} = \frac{k}{d}(\mathbf{v}\cdot\mathbf{e_x}) = \frac{k}{d}\frac{\delta\Phi_x(\xi)}{2\pi\xi},$$
$$\frac{\partial\varphi}{\partial y} = \frac{k}{d}(\mathbf{v}\cdot\mathbf{e_y}) = \frac{k}{d}\frac{\delta\Phi_y(\nu)}{2\pi\nu}, \quad (13)$$

where in this set of equations k stands for the wave number $k = 2\pi/\lambda$. In practice, for a better accuracy in Eq. (12), one uses the frequencies $(\xi_{\text{max}},\nu_{\text{max}})$ corresponding to the peak of maximum cross-spectral power, $\max_{(\xi,\nu)>0}(|H(\xi,\nu)||\tilde{g}_{\text{ref}}(\xi,\nu)|^2)$. In Eq. (11), one can also note that $\delta\Phi = \Phi_{\text{samp}} - \Phi_{\text{ref}}$ with $\Phi_{\text{samp}} = \arg(\tilde{g}_{\text{samp}})$ and $\Phi_{\text{ref}} = \arg(\tilde{g}_{\text{ref}})$.

After calculating the local phase gradients for each pixel, the global reconstruction of the beam phase can be performed by simultaneously integrating the two transverse gradient maps [30,31].

E. Dark-field imaging

The dark-field image, sometimes called the scattering image, is a map of the local decrease of coherence of the beam induced by passing through the sample [8]. With the XGI, the variation of coherence in the section of the beam illuminating a given pixel is calculated by taking the ratio between the fringe amplitude of the sample scan and the reference scan, normalized by the absorption.

From a more general perspective, the partial beam coherence variation affects the amplitude of the interference created

by the wave-front modulation pattern [32]. In other words, the coherence effect translates into the standard deviation of the recorded intensity pattern. Hence, to quantitatively map the coherence decrease C due to the sample scattering properties, one can calculate the ratio of the signal standard deviations between the two scans. Furthermore, this ratio has to be normalized by the absorption to account for the lower number of photons falling on the detector when the sample is inserted in the beam. The values of interest for the two signals are then the normalized standard deviation μ/σ, also known as the coefficient of variation, which leads to the expression of the scattering factor:

$$1 - C = \zeta_{\text{kl}} = \frac{\mu(g_{\text{kl}}^{\text{ref}})}{\mu(g_{\text{kl}}^{\text{samp}})}\frac{\sigma(g_{\text{kl}}^{\text{samp}})}{\sigma(g_{\text{kl}}^{\text{ref}})}. \quad (14)$$

From the definition of σ in Eq. (6) and dropping once again the subscript kl for the sake of clarity, one can write

$$\zeta^2 = \frac{\mu_{\text{ref}}^2}{\mu_{\text{samp}}^2}\frac{\int g_{\text{samp}}^2 - \mu_{\text{samp}}^2}{\int g_{\text{ref}}^2 - \mu_{\text{ref}}^2} = \frac{\mu_{\text{ref}}^2}{\mu_{\text{samp}}^2}\frac{\epsilon_{\text{samp}}^2 - \mu_{\text{samp}}^2}{\epsilon_{\text{ref}}^2 - \mu_{\text{ref}}^2}. \quad (15)$$

F. Measurement of the effective local wave-front curvature

It is sometimes necessary to know the effective second derivative of a wave-front beam, i.e., its local curvature. From Eq. (5), the beam phase second derivative is responsible for the creation of interference in a coherent beam. While this phenomena is used in some propagation techniques sensitive to ΔW, for other applications it can lead to unwanted interference contrast or optical distortions.

As described for the x-ray speckle tracking related technique [18], one can identify different modes when working with near-field speckle. A differential working concept has been described so far, that allows us to isolate the optical transfer function of the sample. Now, to recover the absolute second derivative, one can use the cross-correlation operation between signals collected simultaneously in different pixels. This process has the advantage of not requiring a reference signal and then, when used as such, can be used to monitor the quality of a probing beam.

When performing a raster scan of a surface Γ of a membrane much larger than the pixel size of the detector, the patterns recorded in nearby pixels are very similar. Each pixel will see the same pattern but at different times, as depicted schematically in Fig. 4. If we consider a perfectly collimated beam [Fig. 4(a)], the collected signals in two different pixels (k,l) and $(k+r,l+s)$ of size S_{pix} are connected by

$$g_{k+r,l+s}(x,y) = \Upsilon_{\text{kl}}(r,s)g_{\text{kl}}(x - rS_{\text{pix}}, y - sS_{\text{pix}}), \quad (16)$$

where Υ accounts for the difference of both intensity and coherence in the probing beam at the position of the pixels. We choose to ignore this factor because it accounts for an amplitude modulation factor that does not distort the signal shape.

Similarly, for a noncollimated beam, with different local ray propagation directions, Eq. (16) becomes from Fig. 4(b) with $\chi = \chi_x\mathbf{e_x} + \chi_y\mathbf{e_y}$ the delay between the signals recorded in the two different pixels:

$$g_{k+r,l+s}(x,y) = g_{\text{kl}}(x - \chi_x, y - \chi_y). \quad (17)$$
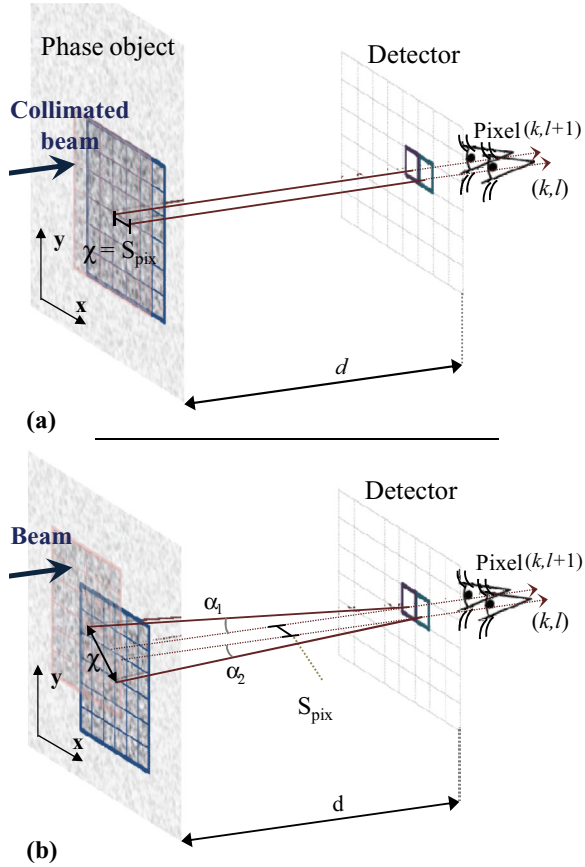
FIG. 4. (Color online) (a) The blue (dark gray) and the red (light gray) area on the phase object represent the pattern seen by two different pixels when scanning this object in a collimated x-ray beam: in this case the pixels are adjacent and $(r,s) = (1,0)$. (b) A similar sketch for the case of a noncollimated beam. The distance χ is defined as the offset between the similar part of the recorded pattern.

Expanding χ from Eq. (16) and using the Fourier shift theorem, we obtain

$$
\tilde{g}_{k+r,l+s} = \tilde{g}_{kl}(\xi,\nu)e^{-i2\pi S_{\mathrm{pix}}(\xi r + \nu s)} \\
\times e^{-i2\pi[\xi(\chi_x - r S_{\mathrm{pix}}) + \nu(\chi_y - s S_{\mathrm{pix}})]}. \quad (18)
$$

While the term in the first exponential matches the distance on the detector separating the considered pixels, the second is related to the local curvature of the beam. Indeed, as we have from Fig. 4(b):

$$
|\chi| = S_{\mathrm{pix}}\sqrt{r^2 + s^2} + d(\alpha_2 - \alpha_1). \quad (19)
$$

Noting $\chi' = \chi - S_{\mathrm{pix}}\sqrt{r^2 + s^2} = \chi - \delta S_{r,s}$ and as for small angles $|\nabla\alpha| = \nabla^2 W(x,y) \approx 1/R(x,y)$:

$$
R \approx \left(\frac{\delta\alpha}{\delta S_{r,s}}\right)^{-1}. \quad (20)
$$

By projection on the transverse vectors $(\mathbf{e_x},\mathbf{e_y})$, the orthogonal local radii are

$$
R_x \approx \frac{dr S_{\mathrm{pix}}}{\chi'_x}, \quad R_y \approx \frac{ds S_{\mathrm{pix}}}{\chi'_y}. \quad (21)
$$

Thus, calculating the shift between signals collected in two nearby pixels, and using the cross-correlation algorithm, one can recover the local second derivative of the beam. Compared to the x-ray speckle tracking technique in absolute mode, this new method is not limited by the magnification of the beam when the distortion of the speckle pattern between images becomes too large. This means that using this stepping mode, larger propagation distances d can be used, providing improved angular sensitivity.

G. The grating case

Grating interferometry is a special case of the technique presented here, where the random probing pattern is replaced with a well known and regular pattern, allowing simplified Fourier analysis [5,33]. For instance, consider the case of the 2D gratings with pitches in the order of 2 to 8 μm for the first phase grating G1 [9]. Approximating the square profile of the grating lines to a sinusoidal shape, the intensity distribution of the pattern produced by the grating interferometer and recorded by the detector in pixel (k,l) can be approximated to

$$
g_{kl}(x,y) = B_1 \cos\left(\frac{2\pi}{P}x + \Phi_x\right)\cos\left(\frac{2\pi}{P}y + \Phi_y\right) + B_2, \quad (22)
$$

with $B_1, B_2, \Phi_x, \Phi_y,$ and P some constants associated to each (k,l). From the transform defined by Eq. (4):

$$
\tilde{g}_{kl}(\xi,\nu) = \sum_{(p,q)\in[\![-1,0,1]\!]} a_{pq}\delta\left(\xi - \frac{p}{P}, \nu - \frac{q}{P}\right), \quad (23)
$$

where δ denotes now the Dirac distribution and where $a_{p,q}$ are complex numbers. One can also note that $a_{0,0} = \mu$. Hence for phase imaging, the cross-correlation operation of Eq. (11) reduces in Fourier space to

$$
g_{\mathrm{samp}} \star g_{\mathrm{ref}} = \tilde{g}^*_{\mathrm{samp}} \cdot \tilde{g}_{\mathrm{ref}} = \sum_{(p,q)\in[\![-1,0,1]\!]} a^{\mathrm{ref}}_{p,q} a^{\mathrm{samp}}_{p,q} *. \quad (24)
$$

Denoting $\Phi_x = \arg(a_{1,0})$, $\Phi_y = \arg(a_{0,1})$, the two components of the transverse displacement of the projected pattern with respect to the reference are

$$
\mathbf{v}_x = \frac{\left(\Phi^{\mathrm{samp}}_x - \Phi^{\mathrm{ref}}_x\right)}{2\pi}P, \quad \mathbf{v}_y = \frac{\left(\Phi^{\mathrm{samp}}_y - \Phi^{\mathrm{ref}}_y\right)}{2\pi}P. \quad (25)
$$

Equation (25) is similar to Eq. (13) when using a single spatial frequency $\xi = \nu = \frac{1}{P}$. Finally, we retrieve the traditional general phase grating interferometer equation in the plane of G1 [9]:

$$
\nabla\varphi \cdot \mathbf{e}_{x/y} = \frac{2\pi}{\lambda}\nabla W \cdot \mathbf{e}_{x/y} = \frac{P}{\lambda}\frac{\left(\Phi^{\mathrm{samp}}_{x/y} - \Phi^{\mathrm{ref}}_{x/y}\right)}{d}. \quad (26)
$$

When using a second absorbing grating G2 with the same orientation as G1, and with a pitch P' very close to P, by the aliasing process, the frequencies of the fringes in one image are rescaled [34]. The superposition of the two patterns created by G1 and G2 generates a new pattern with a larger fringe period equal to $\frac{|P'-P|}{P P'}$, but does not affect the phase distortion induced by the beam. The use of a second grating is motivated by two advantages: it removes or simplifies the phase unwrapping process necessary when employing a single grating; and a detector with larger pixels can be used, enabling usually a larger field of view.

Concerning dark-field imaging with the grating interferometer, the application of formulas (15) to the spectrum of the patterns recorded with the XGI directly leads to the directional scattering imaging formulas already present in the literature [9]:

$$\zeta_x = \frac{\mu_{\text{ref}}}{\mu_{\text{samp}}} \frac{\left|a_{1,0}{}^{\text{samp}}\right|}{\left|a_{1,0}{}^{\text{ref}}\right|}, \zeta_y = \frac{\mu_{\text{ref}}}{\mu_{\text{samp}}} \frac{\left|a_{0,1}{}^{\text{samp}}\right|}{\left|a_{0,1}{}^{\text{ref}}\right|}, \qquad (27)$$

and equivalently for the diagonal directions.

H. Spatial resolution and sensitivity limitations

When using a grating interferometer combined with a high resolving detector, the spatial resolution of the device is limited by the shear distance [5,35]. It is defined, in the plane of G1, by the distance separating two photons interfering in the plane of the detector. In near-field speckle, because all the spatial frequencies of the spectrum contribute to the phase contrast, with an energy transmission predominance in the lower frequencies, the shear effect does not become a limitation when working with random patterns [26]. While the contrast from a phase grating is obtained through the interferences of the zeroth and first diffraction orders, for near-field speckle the contrast is instead obtained from the self-interference scheme [20]. The spatial resolution of the proposed method is then limited by the detector.

However, higher derivatives of the wave front can also have an effect on the spatial resolution of the system. As shown in Fig. 3, the measured angle α of the technique is defined in the plane of the detector. So, when the wave-front gradient is strong, the vector **v** becomes larger than a detector pixel and limits the local spatial resolution. While a short distance d avoids a large vector **v**, it can also affect the wave-front phase sensitivity. One solution to this resolution limitation is to scan the detector instead of the membrane, which requires high-resolution, heavy-duty motion stages. Such a method would actually be an over-sampled version of the x-ray speckle tracking technique [18] where the quantity measured is equivalent to the one obtained with the Hartmann sensor.

The choice of the average speckle grain size is not strict providing that the detector can resolve the features: it only has a small influence on the accuracy of the cross-correlation algorithms that are employed [36]. In any case, various scattering membranes made of small phase objects are commercially available, for instance, as biological filters.

Concerning the angular sensitivity $\delta\theta$ of the deflection measurement, it varies with d and with the smallest measurable vector **v**. Denoting S_{scan} as the piezo scan step and δs as the substep accuracy achievable in the cross-correlation process, the angular sensitivity is $\delta\theta = \delta s\, S_{\text{scan}}/d$. This relation shows that one can optimize the sensitivity of the method either using a larger propagation distance and/or recording images within scans of smaller steps.

Nevertheless, if one opts for diminishing the scanning step size or increasing its number, it should be kept in mind that the number of recorded images increases at a square law rate, equivalently to the 2D XGI. An alternative to this 2D scan image number increase is that when the propagation distance or expected deflection of the wave front is small, one can use the stepping scheme by performing only two
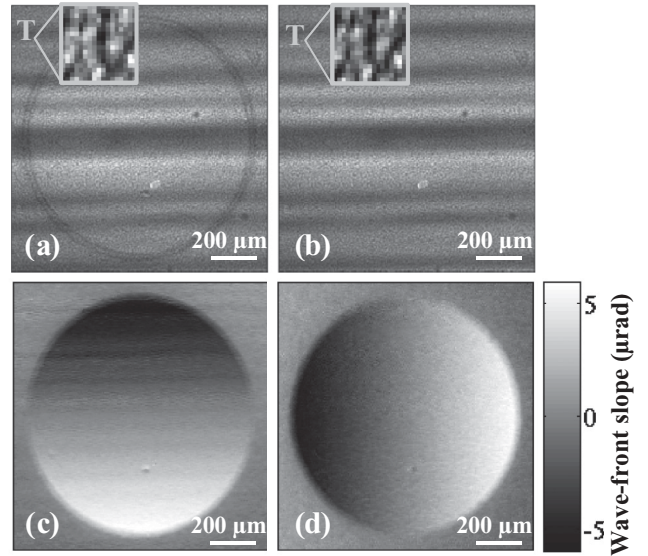
FIG. 5. Differential characterization of a 2D CRL. (a), (b) First image of the scan, respectively, with and without the sample inserted in the beam. The bounded squares show the patterns recorded in each of the scans in the pixel marked T. (c) Horizontal and (d) vertical differential wave-front slopes.

orthogonal scans as with a 1D XGI [37]. This approximation has shown good efficiency when the pattern shift is a fraction of the speckle grain size. The rate of increase law makes the 1D grating interferometer of great interest. Indeed, such a device projects and separates the 2D gradient onto two orthogonal components, rendering the required image number law increasing at an $O(2n)$ rate. This law should be compared to the $O(n^2)$ images law necessary with the 2D XGI or the presented generalized scheme when increasing the steps number for noise robustness and accuracy.

III. EXPERIMENTAL APPLICATION

A set of experiments were performed at the test beamline B16 at Diamond Light Source where the x rays are produced by a bending magnet on the 3 GeV storage ring [38].

A. Numerical implementation aspects

The numerical implementation of the theory described in this paper is a straightforward translation of the equations to discrete space: well known numerical recipes have been used for the implementation of the technique on a standard desktop computer. Considering each pixel (k,l) independently, the intensity signal collected during the scan will describe a 2D pattern $g_{kl}(x_m = mS_x, y_n = nS_y)$ with $(m,n) \in [\![0, M-1]\!] \times [\![0, N-1]\!]$ and (S_x, S_y) are the piezo motor scan steps in the two transverse directions. The calculation of the signal delay described by Eq. (11), necessary for the calculation of the beam local phase shift, can be performed either in real space or Fourier space. In Fourier space, discrete Fourier transforms are typically performed using the fast Fourier transform algorithm which significantly reduces the number of operations and thereby the calculation time. Spectral leakage that can arise from the transformation can be reduced by previous zero
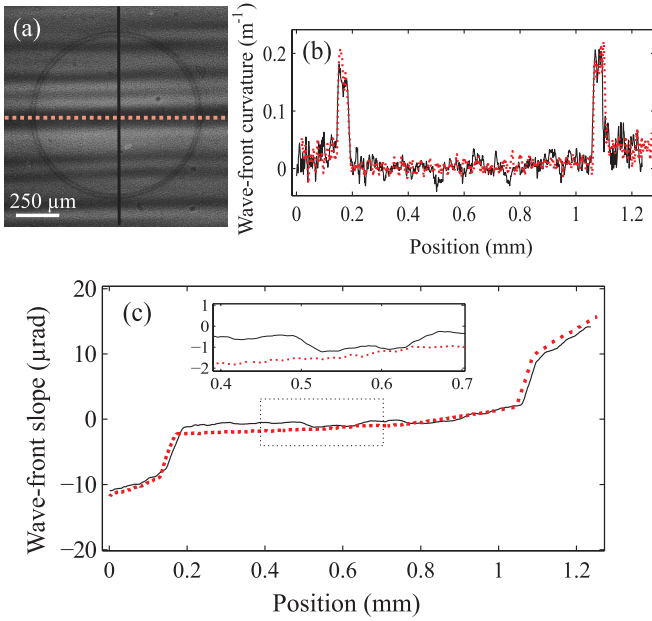
FIG. 6. (Color online) (a) First image acquired during the scan of the membrane. (b) Effective second derivative of the x-ray beam wave-front after propagation through the CRL. (c) Effective wave-front slope obtained by integrating the measured beam's second derivative. The inset shows the effect of the multilayer monochromator phase errors on the amplitude of the fringes. The dashed and plain lines show, respectively, a horizontal and a vertical cut across the CRL.

padding of g. This signal can be then expressed from its 2D Fourier series:

$$g(x_m, y_n) = \frac{1}{MN} \sum_{p,q=0}^{M-1,N-1} a_{p,q} e^{[i2\pi(\frac{pm}{M} + \frac{qn}{N}) + i\Phi_{p,q}]}, \quad (28)$$

and the argument of $a_{p,q}$ can be used for the recovery of the phase, as with the XGI. However, it can be more interesting

to perform the operation described by Eq. (11) in real space, with substep accuracy [36]. This processing method becomes of particular interest when the wave-front gradient is strong, because it allows one to avoid the unwrapping process that can sometimes become problematic.

B. Setup

A double multilayer monochromator, located 15 m from the source, was used to select x rays of an energy $E = 15$ keV ($\Delta E/E \approx 10^{-2}$) which illuminated samples at distance of 50 m from the source. Samples were mounted on a multitranslation and rotation station that allowed easy alignment and removal from the x-ray beam. Another stage on the optics table had several biological filtering membranes mounted on it. Membranes were fixed on a two-dimensional translation piezo motor capable of displacements with nm accuracy. Finally, the last stage of the optics table was occupied by the detector. The camera was a CCD detector imaging an x-ray scintillator through a microscope objective, resulting in a pixel size of 0.9 μm. Care was taken to ensure that the resolution of the detector was sufficient to resolve the speckle features in each image. A schematic of the experiment is shown in Fig. 3.

C. Characterization of a 2D CRL

1. Differential wave-front slope

The technique described in Sec. II D was first applied to the characterization of a 2D compound refractive lens (CRL) to evaluate the quantitative accuracy of the method and for comparison [39,40]. The CRL under test was a single Be refractive lens with an ellipsoidal shape and a design radius at the apex of $R = 200 \mu$m. The theoretical focal length $f = R/2\delta$ of this lens is 66 m [41]. Two orthogonal wave-front gradients induced by the CRL were derived using two sets of 16×16 images acquired while scanning a cellulose acetate membrane of 1 μm size pores. The results are showed in Fig. 5. The focal lengths derived from the measurements are
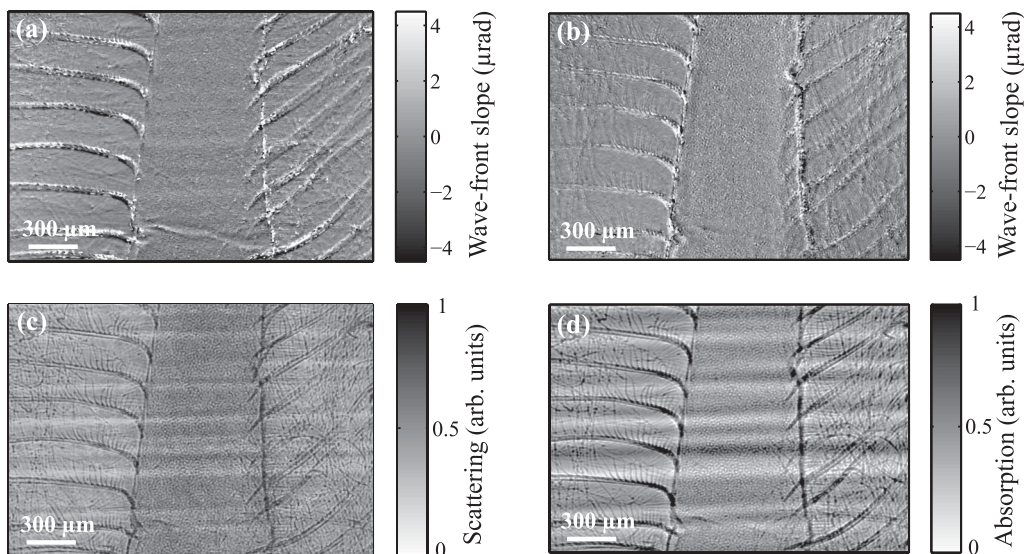
FIG. 7. (a) Vertical and (b) horizontal differential wave-front gradients. (c) Scattering image. (d) Absorption image. One can see in the absorption and scattering images vertical stripes due to the multilayer monochromator instabilities.

65.98 m in the vertical, and 64.87 m in the horizontal plane. While there is very good agreement with the theoretical value in the vertical plane, the values differ by 1.5% in the horizontal. While considering if such a level of error is acceptable, one should remember that the bandwidth of the monochromator was of ∼2%.

In Fig. 4, one can see that no speckle pattern is present in the wave-front gradient maps, as they are only used as an information carrier.

2. Absolute wave-front curvature

To illustrate the efficiency of the method explained in Sec. II F, the local radius of curvature of the beam after passing through the Be CRL lens is plotted in Fig. 6. Despite the high quality of the lens, the wave-front slope of the transmitted beam is not monotonous due to imperfections in the incoming beam, especially in the vertical direction where phase defects from the multilayer monochromator are visible.

These results show the feasibility and validity of the method as a quantitative absolute wave-front measuring tool, which could be used for metrology purposes.

D. Imaging of a feather

As a "real" sample illustration case, the three modal imaging of a bird feather was performed using this technique. The setup was identical to that employed for the characterization of the CRL in Sec. III C. The propagation distance remained at $d = 520$ mm. Two raster scans of 32×32 images were recorded, moving a scattering membrane made of cellulose acetate with 1 μm pore size. Absorption, phase, and scattering images were retrieved from the collected data and the results are displayed in Fig. 7. From the small visible details, one can get an idea of the spatial resolution of the system (pixel size = 0.9 μm) and the fine sensitivity of the method for phase contrast imaging.

IV. CONCLUSION AND PERSPECTIVES

We have demonstrated, theoretically and experimentally, the extension of the three modal imaging scheme from a grating interferometer to a more generalized method that allows the use of any phase objects. The grating case has been shown to be a special case of this general scheme. The proposed technique offers better spatial resolution compared to the XGI, and does not require an x-ray grating, which can be expensive and difficult to purchase for high energy experiments. However, as previously exposed, the XGI and notably the 1D case, still offer noticeable advantages, such as a smaller number of required exposures and a capability to work with a larger field of view.

As a future development, one can already think about using the method in a magnifying geometry to access nm resolutions. Indeed, as one can find grains of any size to generate speckle, the achievable resolution when using a magnifying optic is expected to be pushed down near the diffraction limit. In parallel, the advantage of this technique is that it can be used for very strong gradients, as the unwrapping process can be totally avoided by performing cross correlation in real space. Another idea is to replace the phase object that generates the speckle by a statistical absorption object in order to use the technique with a totally incoherent x-ray beam. We expect that this technique will find many applications for microphase contrast imaging and can be soon exploited in a tomography process to render three-dimensional (3D) objects.

[1] A. Momose, Jpn. J. Appl. Phys. **44**, 6355 (2005).

[2] V. Ronchi, Appl. Opt. **3**, 437 (1964).

[3] S. Yokozeki and T. Suzuki, Appl. Opt. **10**, 1575 (1971).

[4] C. David, B. Nohammer, H. H. Solak, and E. Ziegler, Appl. Phys. Lett. **81**, 3287 (2002).

[5] T. Weitkamp, A. Diaz, C. David, F. Pfeiffer, M. Stampanoni, P. Cloetens, and E. Ziegler, Opt. Express **13**, 6296 (2005).

[6] F. Pfeiffer, T. Weitkamp, O. Bunk, and C. David, Nat. Phys. **2**, 258 (2006).

[7] T. Donath, M. Chabior, F. Pfeiffer, O. Bunk, E. Reznikova, J. Mohr, E. Hempel, S. Popescu, M. Hoheisel, M. Schuster, J. Baumann, and C. David, J. Appl. Phys. **106**, 054703 (2009).

[8] F. Pfeiffer, M. Bech, O. Bunk, P. Kraft, E. F. Eikenberry, C. Bronnimann, C. Grunzweig, and C. David, Nat. Mater. **7**, 134 (2008).

[9] I. Zanette, T. Weitkamp, T. Donath, S. Rutishauser, and C. David, Phys. Rev. Lett. **105**, 248102 (2010).

[10] S. Berujon, H. Wang, I. Pape, K. Sawhney, S. Rutishauser, and C. David, Opt. Lett. **37**, 1622 (2012).

[11] M. Engelhardt, J. Baumann, M. Schuster, C. Kottler, F. Pfeiffer, O. Bunk, and C. David, Appl. Phys. Lett. **90**, 224101 (2007).

[12] K. Creath, in *Progress in Optics*, edited by E. Wolf (Elsevier, Amsterdam, 1988), Vol. 26, pp. 349–393.

[13] C. David, J. Bruder, T. Rohbeck, C. Grunzweig, C. Kottler, A. Diaz, O. Bunk, and F. Pfeiffer, Microelectron. Eng. **84**, 1172 (2007).

[14] E. Reznikova, J. Mohr, M. Boerner, V. Nazmov, and P.-J. Jakobs, Microsyst. Technol. **14**, 1683 (2008).

[15] L. M. Sanchez-Brea and F. J. Torcal-Milla, Appl. Opt. **49**, 2190 (2010).

[16] K. S. Morgan, D. M. Paganin, and K. K. W. Siu, Opt. Lett. **36**, 55 (2011).

[17] A. Olivo and R. Speller, Appl. Phys. Lett. **91**, 074106 (2007).

[18] S. Bérujon, E. Ziegler, R. Cerbino, and L. Peverini, Phys. Rev. Lett. **108**, 158102 (2012).

[19] K. S. Morgan, D. M. Paganin, and K. K. W. Siu, Appl. Phys. Lett. **100**, 124102 (2012).

[20] R. Cerbino, L. Peverini, M. A. C. Potenza, A. Robert, P. Bosecke, and M. Giglio, Nat. Phys. **4**, 238 (2008).

[21] J. Goodman, *Introduction to Fourier Optics*, 3rd ed. (Roberts and Company Publishers, Greenwood Village, CO, 2005).

[22] P. Cloetens, J. P. Guigay, C. De Martino, J. Baruchel, and M. Schlenker, Opt. Lett. **22**, 1059 (1997).

[23] T. E. Gureyev, D. M. Paganin, A. W. Stevenson, S. C. Mayo, and S. W. Wilkins, Phys. Rev. Lett. **93**, 068103 (2004).

[24] K. A. Nugent, T. E. Gureyev, D. F. Cookson, D. Paganin, and Z. Barnea, Phys. Rev. Lett. **77**, 2961 (1996).

[25] M. R. Teague, J. Opt. Soc. Am. **72**, 1199 (1982).

[26] J. W. Goodman, *Speckle Phenomena in Optics; Theory and Applications*, 1st ed. (Roberts and Company Publishers, Greenwood Village, CO, 2006).

[27] P. Mercere, S. Bucourt, G. Cauchon, D. Douillet, G. Dovillaire, K. A. Goldberg, M. Idir, X. Levecq, T. Moreno, P. P. Naulleau, S. Rekawa, and P. Zeitoun, in *Advances in Metrology for X-Ray and EUV Optics*, edited by L. Assoufid, P. Z. Takacs, and J. S. Taylor, Proc. SPIE 5921 (SPIE, Bellingham, WA, 2005) p. 592109.

[28] M. V. R. K. Murty and E. C. Hagerott, Appl. Opt. **5**, 615 (1966).

[29] *Handbook of Optical Metrology: Principles and Applications* (CRC Press, Yokohama, Japan, 2009), p. 744.

[30] W. H. Southwell, J. Opt. Soc. Am. **70**, 998 (1980).

[31] R. T. Frankot and R. Chellappa, IEEE Trans. Pattern Anal. Mach. Intell. **10**, 439 (1988).

[32] J. W. Goodman, *Statistical Optics* (John Wiley and Sons, New York, 1985).

[33] K. A. Goldberg and J. Bokor, Appl. Opt. **40**, 2886 (2001).

[34] K. Creath and J. C. Wyant, in *Optical Shop Testing*, 2nd ed., edited by D. Malacara (Wiley, New York, 1992), pp. 653–685.

[35] K. Iwata, Appl. Opt. **48**, 886 (2009).

[36] B. Pan, K. Qian, H. Xie, and A. Asundi, Meas. Sci. Technol. **20**, 062001 (2009).

[37] C. Kottler, C. David, F. Pfeiffer, and O. Bunk, Opt. Express **15**, 1175 (2007).

[38] K. J. S. Sawhney, I. P. Dolbnya, M. K. Tiwari, L. Alianelli, S. M. Scott, G. M. Preece, U. K. Pedersen, and R. D. Walton, AIP Conf. Proc. **1234**, 387 (2010).

[39] M. Engelhardt, J. Baumann, M. Schuster, C. Kottler, F. Pfeiffer, O. Bunk, and C. David, Rev. Sci. Instrum. **78**, 093707 (2007).

[40] S. Rutishauser, I. Zanette, T. Weitkamp, T. Donath, and C. David, Appl. Phys. Lett. **99**, 221104 (2011).

[41] *X-Ray Data Booklet*, edited by D. Vaughan (Center For X-Ray Optics, Lawrence Berkeley Laboratory, University of California, Berkeley, CA, 1985), Tables 5-2.